2 PF Ring

2-1 Summary of Machine Operation

The PF ring was closed on February 28, 2005 for reconstruction work for the Straight-Section Upgrade Project. It was reopened for commissioning after the completion of reconstruction on September 20, 2005. User experiments restarted on October 18 as seen in Fig. 1. The details of the Straight-Section Upgrade Project and the progress of the commissioning are reported in the following section. Table 1 shows the operation statistics of the PF ring for FY2005. Figure 2 shows the ring operation time, scheduled user time and actual user time since 1982. The total operation time of 3720 hours in FY2005 was noticeably shorter than recent years, since the ring was shut down for seven months. The scheduled user time was 2640 hours and the actual user time was 2572 hours excluding time losses due to machine trouble and daily injections. The ratio of actual user time to scheduled user time has been maintained at 96-98% for the past 6 years. Figure 3 shows the product $I\tau$ (I is the beam current and τ the beam lifetime) over the past 9 years. The reduced $I\tau$ after the reconstruction has gradually recovered as seen in the figure. Figure 4 shows the history of the average stored beam current since 1982. In order to keep the average beam current following reconstruction as high as possible, the injection frequency was increased from once per day (the usual injection frequency before reconstruction) to two or three times per day as described below. The change in the failure rate, defined as the ratio of the failure time to the total operation time, is shown in Fig. 5. The failure rate which was about 1% through the 1990's has been kept at around 0.5% for the past 4 years. This high reliability has been realized by the sustained efforts of the staff in the Light Source Division and the operators to keep the machine in good condition. However a serious vacuum fault with an SR absorber was encountered at the end of March 2006, a failure that is attributed to "superannuation". Fortunately, the trouble was settled immediately. Some old components are still in use in several sections, but many have been renewed as part of the Straight-Section Upgrade Project.

For the usual multi-bunch operation at 2.5 GeV, the ring was injected three times a day from October 18 to November 21, 2005, and twice a day from November 22. This was necessary because the beam lifetime was reduced following the renewal of many vacuum components in the Straight-Section Upgrade Project. The initial beam current of 450 mA was unchanged throughout FY2005. In single-bunch mode, an injection frequency of three times a day was used prior to reconstruction. Following reconstruction, however, the bunch length was shortened, resulting in a decreased lifetime due to a decrease in the coupling impedance of the vacuum system with the improved vacuum components. It was thus necessary to increase the injection frequency to 6-8 times a day, although the initial beam current of 70 mA was unchanged (except for the first trial at 60 mA). In a 3-GeV mode the beam current was restriced to 200 mA, due to the limited RF power available as before the reconstruction.

The KEK linear accelerator distributes electron/positron beams to four storage rings: the KEKB HER (high-energy ring: 8-GeV e^-), the LER (low-energy ring: 3.5-GeV e^+), the PF and the PF-AR. The switching speed among injection modes of these four rings had previously been a big limitation of the beam distribution system. As part of the simultaneous injection project described in the previous issue of this report, a fast beam-switching system had been partly realized, resulting in a significant improvement in switching speed. Top-up injection of the PF ring will be soon realized, as described in the following section.

Table 1 Operation statistics of PF Ring in FY2005.

	Multi-bunch	Single-bunch	Total
Ring operation time (hours)	3432.0	288.0	3720.0
Scheduled user time (hours)	2352.0	288.0	2064.0
Actual user time T (hours)	2298.0	274.4	2572.4
Time used for injection (hours)	34.1	12.6	46.7
Integrated current in T (A·hours)	807.7	9.9	817.6
Average current in T (mA)	351.5	36.1	--
Number of injections	223	79	302
Interval between injections (hours)	10.3	3.5	--

Timetable of the Machine Operation in FY 2005

	SUN 9 17	MON 9 17	TUE 9 17	WED 9 17	THU 9 17	FRI 9 17	SAT 9 17	SUN 9 17	MON 9 17	TUE 9 17	WED 9 17	THU 9 17	FRI 9 17	SAT 9 17	SUN 9 17	MON 9 17	TUE 9 17	WED 9 17	THU 9 17	FRI 9 17	SAT 9 17
Date	**3.27**	28	29	30	31	**4.1**	2	3	4	5	6	7	8	9	10	11	12	13	14	15	16
PF																					
AR																	B				
Date	17	18	19	20	21	22	23	24	25	26	27	28	29	30	**5.1**	2	3	4	5	6	7
PF																					
AR			B							B											
Date	8	9	10	11	12	13	14	15	16	17	18	19	20	21	22	23	24	25	26	27	28
PF																					
AR			B							B							B				
Date	29	30	31	**6.1**	2	3	4	5	6	7	8	9	10	11	12	13	14	15	16	17	18
PF																					
AR			B							B							B				
Date	19	20	21	22	23	24	25	26	27	28	29	30	**7.1**	2	3						
PF																					
AR			B							B											
Date	**9.18**	19	20	21	22	23	24	25	26	27	28	29	30	**10.1**	2	3	4	5	6	7	8
PF																					
AR																	B				
Date	9	10	11	12	13	14	15	16	17	18	19	20	21	22	23	24	25	26	27	28	29
PF										B							B				
AR			B							B							B				
Date	30	31	**11.1**	2	3	4	5	6	7	8	9	10	11	12	13	14	15	16	17	18	19
PF			B							B							B				
AR			B							B							B				
Date	20	21	22	23	24	25	26	27	28	29	30	**12.1**	2	3	4	5	6	7	8	9	10
PF			B							B(SB)							B				
AR			B							B							B				
Date	11	12	13	14	15	16	17	18	19	20	21	22	23	24	25	26	27	28	29		
PF			B							B											
AR			B																		
Date	**1.15**	16	17	18	19	20	21	22	23	24	25	26	27	28	29	30	31	**2.1**	2	3	4
PF										B							B				
AR										B							B				
Date	5	6	7	8	9	10	11	12	13	14	15	16	17	18	19	20	21	22	23	24	25
PF			B(SB)							B							B				
AR			B							B							B				
Date	26	27	28	**3.1**	2	3	4	5	6	7	8	9	10	11	12	13	14	15	16	17	18
PF			B							B							B				
AR			B							B							B				
Date	19	20	21	22	23	24	25	26	27	28	29	30	31	**4.1**	2	3	4	5	6	7	8
PF																					
AR																					

PF: PF ring

AR: PF-AR

Tuning and ring machine study

Short maintenance and /or machine study

Machine & BL study

Ring machine study

Experiment using SR

Single bunch operation at 2.5 GeV

Multi bunch operation at 3.0 GeV

Figure 1
Timetable of machine operation in FY2005.

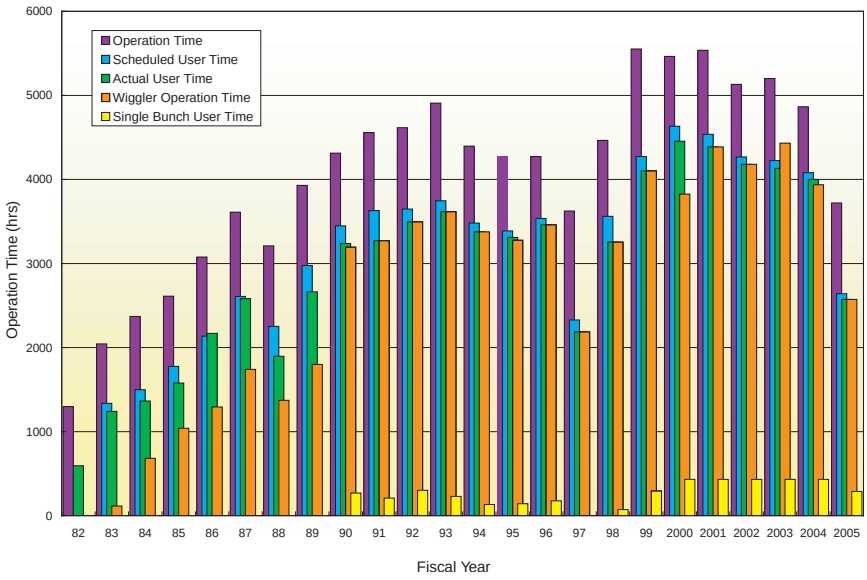

Figure 2
Operation time history of the PF Storage Ring.

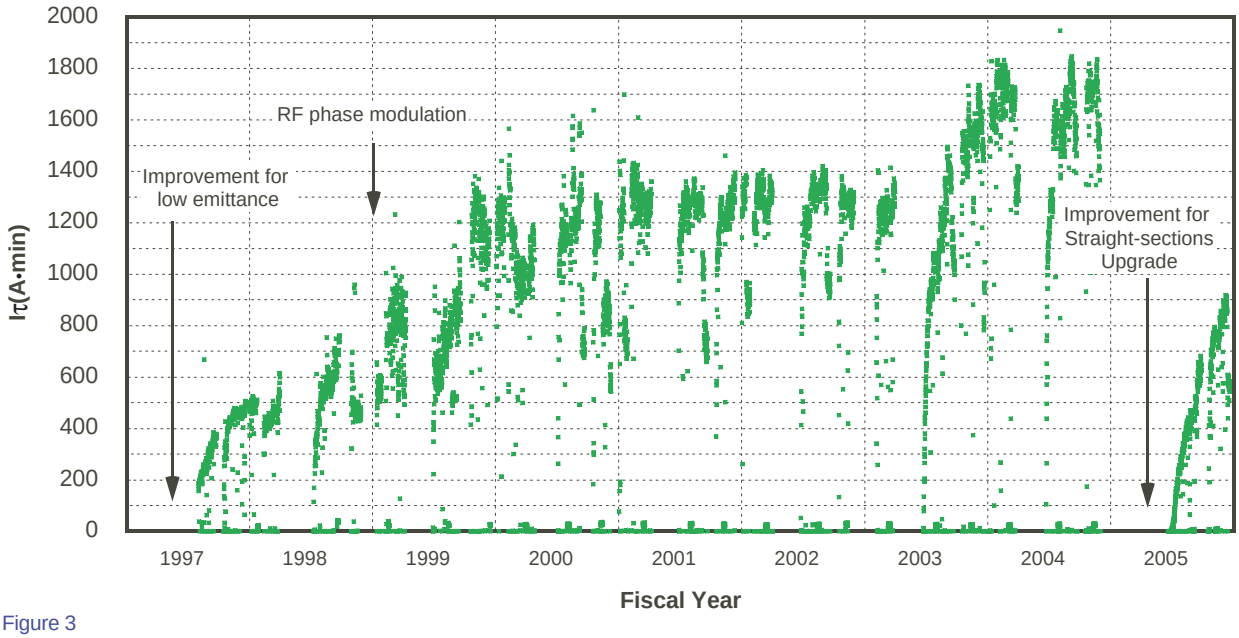

Figure 3
$I\tau$ history of the PF Storage Ring over the past 9 years.

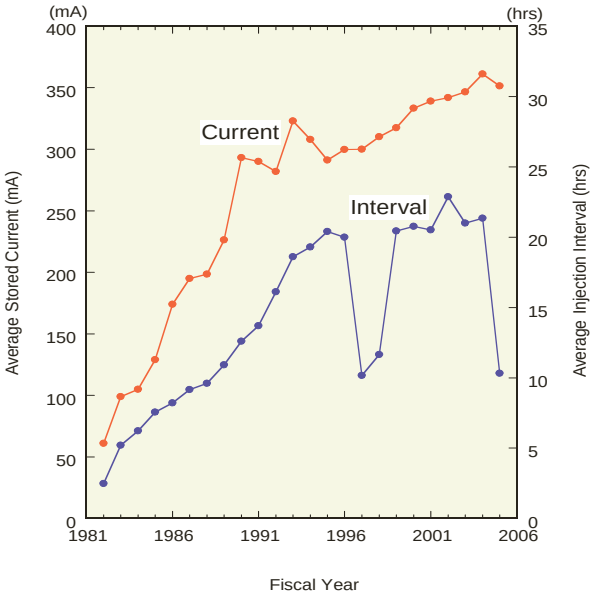

Figure 4
Average stored current and injection interval since 1982.

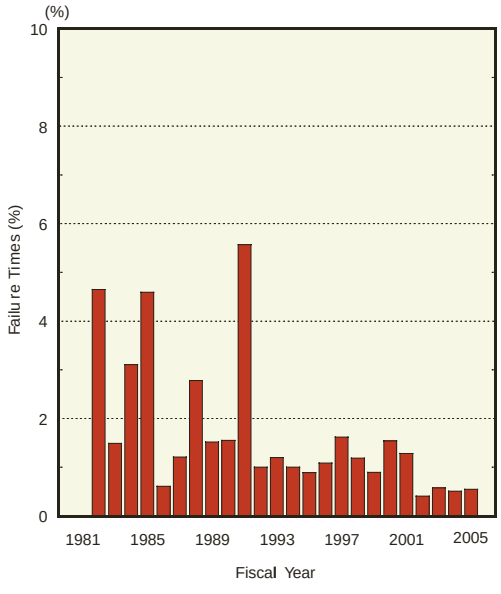

Figure 5
Failure rate history.

2-2 Straight-Section Upgrade Project

For the straight-section upgrade project, a major reconstruction of the 2.5-GeV ring was completed with a seven-month intermission in user experiments in 2005. As a result of the reconstruction, four new straight sections have been created and ten existing straight sections have been extended. A short-gap mini-pole undulator with high brilliance in the hard X-ray range has been installed in one of the new straight sections. Recommissioning began at the end of September 2005, and user experiments were resumed a month later. Although no *in-situ* baking was carried out for the newly installed beam ducts, the beam lifetime has progressively recovered due to vacuum scrubbing by the synchrotron radiation.

Reconstruction of the storage ring

The reconstruction work of the storage ring was conducted during the scheduled March-to-September shutdown in 2005. The magnetic configurations of the straight sections, shown in Fig. 6, have been modified by replacing all of the quadrupole (Q) magnets. The bending (B) magnets and the existing insertion devices including the RF cavities have been left untouched. All of the Q ducts were replaced, in line with the rearrangement of the Q magnets and the reduction of their bore diameter. Twelve B ducts were renewed and the synchrotron radiation ports of the B ducts were made compatible with new or future insertion-device beamlines.

The pumping speed of the distributed ion pumps in the B duct has been improved by 80% by renewal of the pumping cells and by increasing the applied voltage. The main material of the crotch absorbers has been upgraded to heat-resistant copper alloy from OFHC copper. The small gaps between the ICF flanges which caused an impedance increase have been smoothed using RF contacts, and the old vacuum bellows without RF shields have been almost entirely removed from the storage ring.

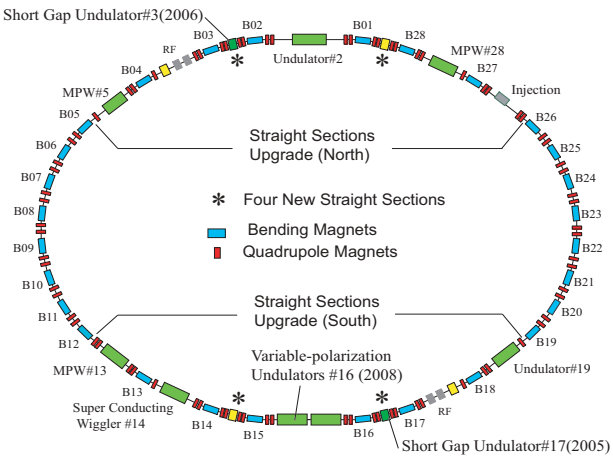

Figure 6
Reconstructed area for the straight sections upgrade of the PF ring.

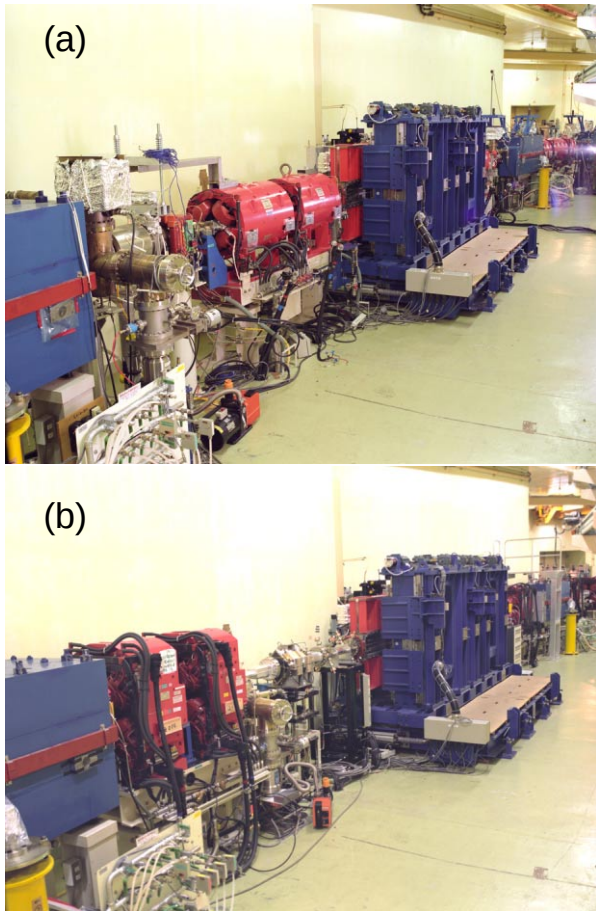

Figure 7
Straight section for the undulator #2, before upgrade (a) and after the upgrade (b).

Figure 8
Installation of SGU#17.

Thirteen beamline front ends related to the straight sections have been remodeled. The replacement of front ends has been continued using the normal shutdown periods in spring and summer since 2002.

The lengths of the extended straight sections and the newly created four straight sections are summarized in Table 2. The photographs of Fig. 7 show the section between B01 and B02 before and after the reconstruction. A planar undulator U#2 with a 4-m magnetic length will be installed in this section. The original length of 5 m has been extended to 8.9 m, and the newly created free space between the U#2 and the doublet magnets is about 2 m at either end of U#2.

The new short straight sections are used for short-

Table 2 Creation and extension of the straight sections and the upgrade plan of the insertion devices.

Section	Before upgrade	After upgrade	Insertion devices
B01 – B02 B15 – B16	5.0 m	8.9 m	Undulator#02 Variable-polarization U (planning)
B03 – B04 B13 – B14 B17 – B18 B27 – B28	4.3 m	5.4 m	RF cavities Superconducting wiggler RF cavities Elliptical U/MPW#28
B04 – B05 B18 – B19	3.5 m	5.3 m	MPW#5 U#19 (Revolver)
B12 – B13 B26 – B27	4.3 m	5.4 m	U/MPW#13 Injection
B02 – B03 B14 – B15 B16 – B17 B28 – B01	0 m	1.4 m	Short gap undulator#03 (2006) Short gap undulator#17 (2005)

gap mini-pole undulators (SGU). The vertical β function at the short straight section is reduced to 0.4 m for the very short-gap in-vacuum undulators. Even with a medium energy of 2.5 GeV, high-brilliance hard X-rays are available using the mini-pole undulators. The first mini-pole undulator was installed in 2005 at one of the newly created straight sections between B16 and B17 (SGU#17). It has a magnetic period of 16 mm, a periodicity of 29 and a designed minimum gap of 4.5 mm. Figure 8 is a photograph of SGU#17 during its installation. The second SGU, with a magnetic period of 20 mm, is scheduled to be installed at BL#3 in 2006.

Commissioning and beam operation

Recommissioning of the storage ring was started at the end of September 2005. The maximum stored current could be restored to the typical value of 450 mA in five days as shown in Fig. 9, although the beam lifetime at first was less than 30 minutes and the beam showed strong ion instabilities. With the deterioated vacuum of the order of 10^{-5} Pa, stable beam injection became possible by introducing a transverse bunch-by-bunch feedback system. Along with orbit correction and adjustment of other beam parameters, vacuum scrubbing at the maximum current of 500 mA was continued. Following one month of commissioning, user operation resumed with a beam lifetime of 200 A·min, or about 8 hours at 450 mA.

During commissioning, X-rays emitted from the in-vacuum undulator SGU#17 were successfully introduced to the beamline. It was confirmed that a minimum gap of 3.8 mm could be achieved, slightly narrower than the designed value.

One of the merits of the PF ring has been its long beam lifetime. The product of the beam lifetime and the beam current, Iτ, exceeded 1600 A·min just before the reconstruction. As shown in Figs. 10 and 11, in the six-months of operation following the reconstruction, the lifetime has recovered to 900 A·min, about 60% of the previous value. No *in-situ* baking of the beam ducts was carried out following installation. In order to investigate the effects of pre-baking on the vacuum scrubbing, the beam ducts for the south sections were pre-baked in advance of the installation, and those for the north sections were not pre-baked at all. At the very first stages of beam operation, while the integrated current was less than several tens of A·h, a slight difference remained between the vacuum pressures in the north sections and in the south sections. No significant differences were subsequently observed.

Before and after the reconstruction, typical spectra observed as the transverse instability were changed. The PF ring is operated usually at an initial current of 450 mA with a partial filling pattern. Consecutive 280

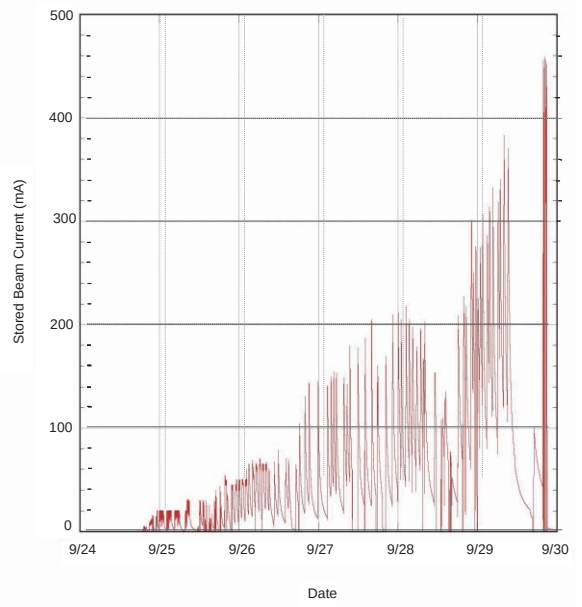

Figure 9
Increase of the stored current during the first 5days of commissioning.

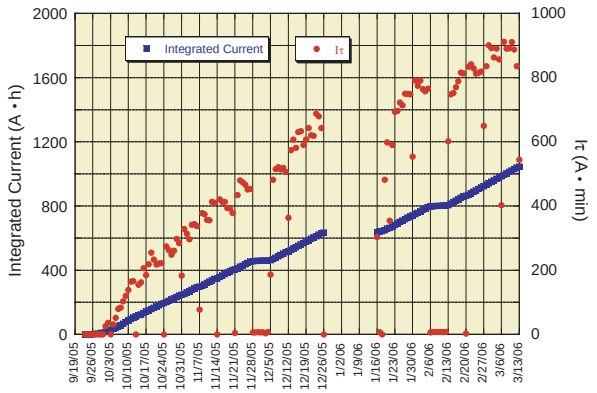

Figure 10
Progress of integrated stored current (A·h) and product of beam current and lifetime Iτ (A·min) during the six months following commissioning.

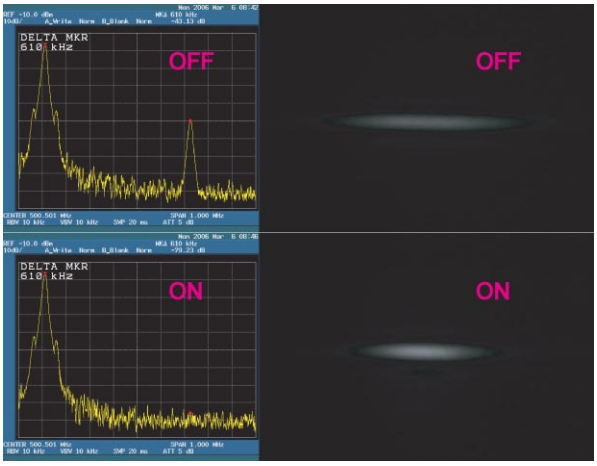

Figure 13
Beam spectrum observed as the horizontal instability and SR beam profile with bunch-by-bunch feedback ON/OFF. The span of the spectrum is 1 MHz and the maximum peak is the RF frequency at 500.1 MHz.

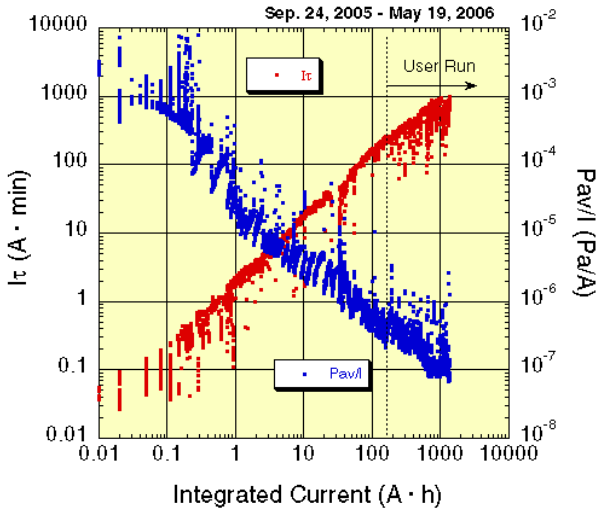

Figure 11
Iτ and the average pressure normalized by the stored current as a function of the integrated stored current.

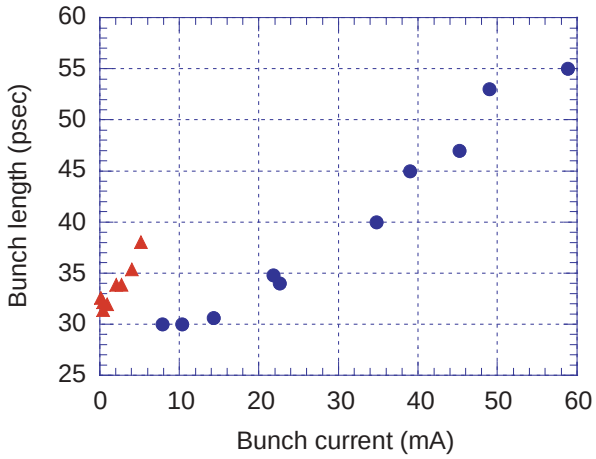

Figure 14
Comparison of bunch lengthening before (red triangles) and after (blue circles) the upgrade.

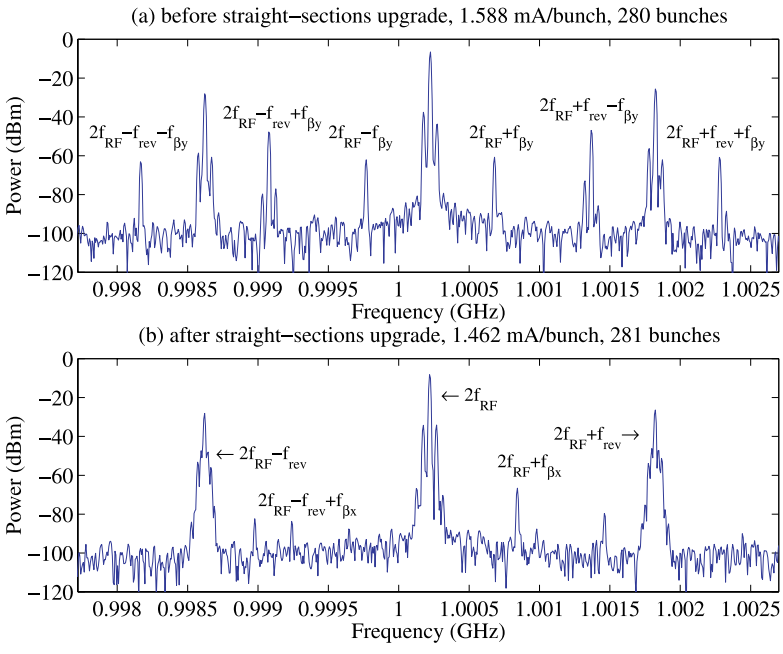

Figure 12
Betatron sidebands observed in the usual partial filling mode changed from vertical (a) to horizontal (b) after the upgrade.

bunches are filled with electrons and 32 bunches remain unfilled to avoid a strong instability due to ion trapping. Even with partial filling, a weak transverse instability which is also assumed to be an ion instability occurs at a current of 450 mA. As shown in Fig. 12(a), only the vertical betatron sidebands were observed previously. However, after the reconstruction, horizontal betatron sidebands were observed instead of the vertical sidebands. The betatron tunes for both directions changed from (ν_x, ν_y) = (9.60, 4.28) to (9.60, 5.28), so the fractional tunes have the same values. The horizontal instability could completely be suppressed by using the transverse bunch-by-bunch feedback system during user operation as shown in Fig. 13. Experimental studies and an analysis of the transverse instability will continue.

Figure 14 shows a comparison of the current-dependent bunch length before and after the reconstruction. Previously bunch lengthening was observed at even very low bunch currents. After reconstruction the threshold for bunch lengthening has increased to above 10 mA. This is a result of the reinforcement of the RF shield in the beam ducts. As the bunch is effectively shortened at practical currents, the beam lifetime during single bunch operation (which is limited by the Touschek lifetime) is now one-third of its previous value.

2-3 Research of Top-Up Project

The top-up operation project

Operation of the storage ring by top-up or continuous injection is now very important at the SR facilities. This mode of operation of the storage ring provides keeping the constant intensity of SR for the users and a constant heat load on the optical components of the beamlines. Top-up injection not only enables keeping the SR intensity constant but also allows us to be free from the serious lifetime problem due to small beam size in small emittance operation, and the problem of toucheck effect in low-energy rings etc. At the KEK, a linac upgrade project is now in progress. This project involves the realization of a pulse-by-pulse multi-energy acceleration of the beam in one linac (8 GeV for HER of B Factory (KEKB), 3.5 GeV for LER of B Factory, and 2.5 GeV for Photon Factory). Using this scheme will make it possible to inject the beam into both the B Factory and the Photon Factory with pulse-by-pulse switching of the beam. This project will partially finish until autumn 2006, after which it will be possible to make injection to the Photon Factory without disturbing the operation of the B Factory. We plan to operate the PF storage ring in top-up injection mode from the operation in autumn 2007.

In the recent progress of the top-up injection project, a new beam-transport (BT) line has been constructed and injection with the beam from the A1 gun has been tested. Further machine studies of the multi-energy linac scheme have been performed. To realize the operation of the ring with top-up injection mode, a coherent oscillation of the stored beam which is excited by an error in the injection pulse bump is one of serious problems. The status of new beam-transport line and the progress in the optimization of the injection pulse bump are described in this chapter.

Status of the new beam-transport line

–Injector upgrade plan

The KEK Linac is a 600-m-long injector for the four rings (PF, PF-AR, KEKB e^- and e^+ storage rings), which need the beams with the different energies and charges. The injector upgrade was started in the summer of 2005 since the PF top-up and the KEKB continuous injection should be carried out at the same time in the future operation. The injector linac will be upgraded to perform the fast beam-mode switching up to 50 Hz so that each beam pulse can be delivered to the desired ring. The injector upgrade will be carried out by the following three phases:

(1)Phase I: Construction of a new PF beam-transport (BT) line (completed in the summer 2005)
(2)Phase II: Simultaneous injection of electron beams for the PF and the KEKB
(3)Phase III: Simultaneous injection for all the four rings

•*Construction of the new PF-BT line*

In the summer of 2005, we constructed the new 60-m-long BT line, in which the new DC bend (BM_58_1) was installed to deflect the electron beam from the end of Linac to the new line. A photograph and the layout of the new BT are shown in Figs. 15 and 16, respectively. The new BT bypasses the ECS (Energy Compression SYStem) magnets and the former switch bend is placed downstream of the ECS magnets.

The new PF-BT consists of three bending magnets, four quadrupole magnets (quads) and three steering magnets. All magnets installed in the new BT can be also used for the 3-GeV beam operation. The bending magnets are reused from those of the old TRISTAN-AR beam-transport (AR-BT) line. They are H-type conventional block magnets. It takes 30 s to rise the magnetic

Figure 15
View of the new PF-BT.

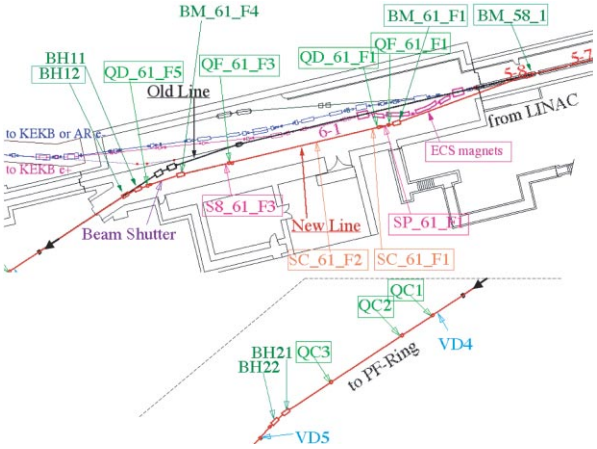

Figure 16
Layout of the new PF-BT.

field from zero to the operation field (~ 0.92 T), and there is a remanent field of 33 G. For the KEKB mode, the main current of BM_58_1 is turned off and the correction coil of this magnet is excited to 0.78 A in order to cancel the remanent field. In addition, the μ metal shield was applied for the vacuum chambers to avoid a weak magnetic-field leakage from the ECS bends.

Two types of quadrupole magnets are used for the new BT. Two of the upstream quads are reused from the old AR-BT line, whose bore diameter is 52 mm. The poles of these magnets were remade to fit the bore diameter of the quads in the PF line, which is 63 mm. The two downstream quads and all the steering magnets are moved from the old PF-BT line. The stabilities of the power supplies are less than 100 ppm in peak-to-peak (p-p), and the ripples of them less than 50 ppm (p-p). The magnets installed in the new BT were aligned using a laser tracker that can measure the magnet position with accuracy of 1 μm. Each magnet was settled within an error of about 100 μm. These values are sufficiently small to correct the beam orbit with the steering magnets.

•*Dispersion correction*

The design optics including β functions, dispersion functions and beam sizes with an energy spread of 0.125% are shown in Fig. 17. The blue and red curves refer to the horizontal and vertical planes, respectively. The dispersion function at a profile monitor (SC61F2) is designed to be zero. In the actual operation, however, a change in beam energy produced an orbit shift of a few mm as observed on the SC61F2 profile monitor. The observed dispersion errors could be attributed to strength errors of quads in the region where the horizontal dispersion functions are not zero. We made measurements of the correction factors for the quads using the beam. For these measurements quads were divided into two groups, i.e., quads which are in the upstream of BH12 (Group-1) and the others (Group-2). Because the currents of quads in the two groups are set using the different excitation curves, which are not cross-calibrated, there should be at least two independent correction factors for the quads.

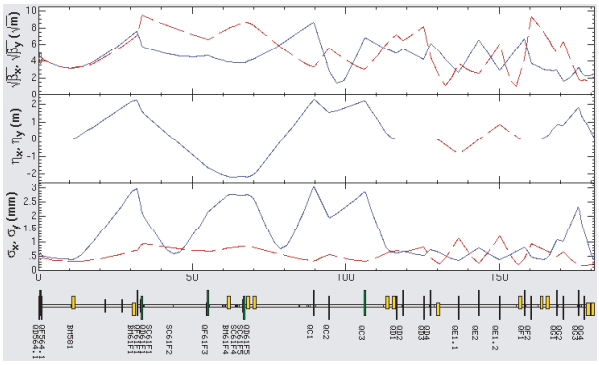

Figure 17
Design optics parameters of PF-BT.

There are four quads (QF61F1, QD61F1, QF61F3 and QD61F5) upstream of BH12. BPMs are installed adjacent to each quads. To prevent scaling errors of BPMs from affecting the results, we employed a special optics where the horizontal dispersion function at a BPM (S861F3) located just downstream of QF61F3 is zero. The dispersion function at S861F3 depends on the three quads upstream of it. By varying the correction factor common to these three quads, we measured the dispersion at the BPM. We obtained the correction factor of 0.9536 for the quads, leading to a dispersion of −0.0041±0.002. Without the correction factor, it was −0.178±0.002. The correction factor for QD61F5 was assumed to be the same value as for the others.

There are three quads (QC1, QC2, QC3) downstream of BH12 in the region where the horizontal dispersion function is not zero. Prior to the measurement we set up the initial design optics (Fig. 17) with a correction factor applied to the quads of Group-1. In order to detemine the dispersion function at the BPMs, we measured the BPM response to the beam energy varying within ±0.2%. We made a least-square fit to minimize the difference between the measured dispersion and the design values, taking the correction factor of the quads for free parameters. Because the three quads are cross-calibrated, the correction factors are considered to be identical. Due to scanning errors, we cannot find a solution to a unique correction factor for these three quads. We assumed that the three quads have independent correction factors. The results are summarized in Table 4. We did not make corrections for the quads downstream of QC3 this time, because the dispersion functions are zero in this region. The measured dispersion function with correction factors applied is shown in Fig. 18. The measured horizontal dispersion functions (EX in the top row) are in good agreement with the design values (η_x in the third row).

Tabel 4 Correction factors of quads.

	Correction factors
Quads above BH12	0.9536
QC1	1.0127
QC2	0.9845
QC3	1.0782

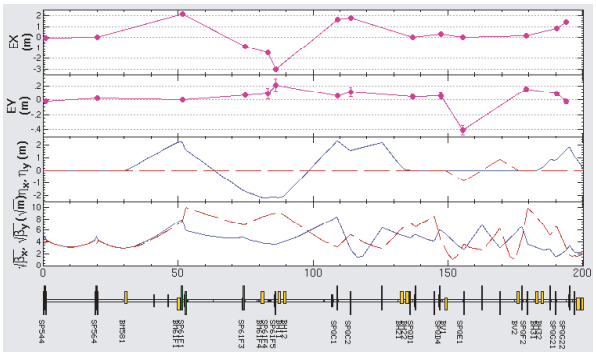

Figure 18
Measured dispersion function after setting the correction factors in Table 1 to the quads.

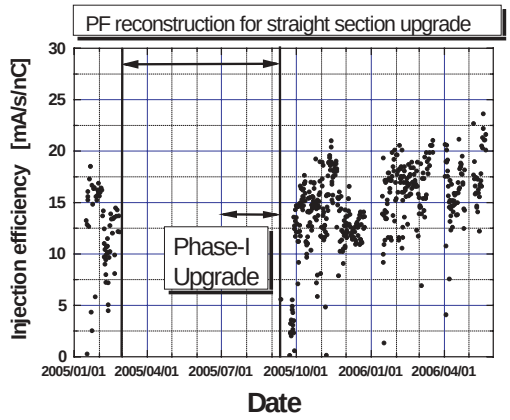

Figure 19
Injection efficiency history.

The new PF-BT is very effective for shortening the beam-mode switching time since the new BT does not need standardization of the ECS bends for the beam-mode change from KEKB to PF and vice verse. Moreover, the injection efficiency has increased and become more stable after the Phase-I as shown in Fig. 19. The improvement of the PF injection was carried out by a magnetic shielding and a dispersion correction.

•*Machine study for Phase-II*

Phase-II aims at realizing the fast beam-mode switching between the KEKB e^- and PF modes. Here, we will use the characteristic scheme called "Multi-Energy Linac". In this scheme, the common magnet settings are used since the current DC magnet system cannot enable a fast field switching for the different beam mode. The fast change of the beam energy is carried out by the rapid control of the low-level RF phases. The optics difference is caused only by the energy difference of each mode. Although the PF injection requires an electron beam with 2.5 GeV, the beam is accelerated up to around 5 GeV in the Multi-Energy Linac scheme to restrain the orbit deterioration caused by the wake-field. After then, the beam energy is adjusted to 2.5 GeV by using the deceleration RF phases. A preliminary machine study using the multi-energy scheme was carried out, and its result shows that the emittance and the beam orbit are sufficiently good for both modes. In a study of the PF injection using the common magnet settings, the beam injection rate is almost constant in daily operation. It has been confirmed that this scheme is feasible for the real operation.

In FY2006, we will replace the DC bend (BM_58) by a pulsed bend. After installation of a pulsed bend, a detailed machine study will be going on for the simultaneous injection for the PF and the KEKB e^- injection modes. Towards the complicated operation, the timing system of the injector LINAC will be upgraded in the near future. A new BPM-DAQ system also will be installed for a fast beam-orbit measurement up to 50 Hz.

Compensation of coherent oscillation of the stored beam

A coherent oscillation of the stored beam is often excited by an error in the injection-pulse bump. Since these oscillations are excited every injection period, they cause a serious problem for top-up operation of the storage ring. In 2004 we investigated the coherent oscillation due to a kick error of the injection kicker magnets, using an SR monitor system with a fast-gated camera [1]. The source point of this monitor is in B27, the second bending magnet in the injection bump. The coherent oscillations in the 16 turns following excitation of the kicker magnets were recorded in one frame of the fast-gated camera. We observed oscillations at the excitation timing from the head to bottom of the pulse every 200 ns. The relation between excitation timing and pulse shape is schematically shown in Fig. 20.

Oscillations of the stored beam following optimization of the injection-pulse bump can be seen in the beam-position images shown in the left column of Fig. 21. The beam spots on the left-hand side of the images are due to the beam which appears just at the timing of the injection bump. The horizontal oscillations at each excitation timing are almost suppressed in all the excitation timings. Through all observations, we detected vertical oscillations of the stored beam, even when the horizontal oscillation is suppressed. We attribute this vertical oscillations to rotational errors in the alignment of the quadrupole magnet. During the summer shut down of 2005, we aligned all of the quadrupole magnets

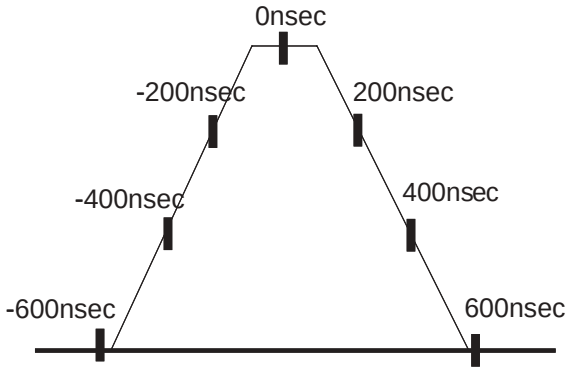

Figure 20
The relation between timing measuring points and the pulse shape of the injection bump.

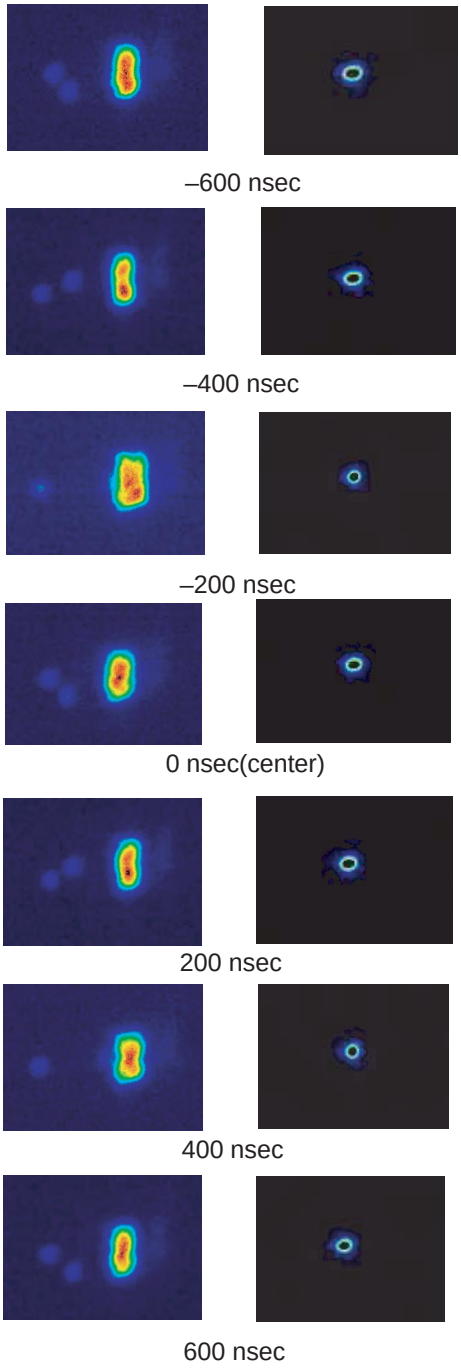

Figure 21
Observed beam oscillations before alignment of the ring quadrupole magnets (left column) and after the alignment (right). 16 turns are superimposed in each frame. The weak beam spots on the left-hand side of the images in the left column are due to the beam which appears just at the timing of the injection bump.

in the ring, followed by re-optimization of the injection bump. Beam images showing oscillations of the stored beam following this alignment are shown in the right-hand column of Fig. 21. The vertical oscillations are almost suppressed, and the remaining small horizontal oscillations are also suppressed compared to those before the alignment.

References

[1] A. Ueda, T. Mitsuhashi, K. Harada and Y. Kobayashi, *Proc. EPAC04,* (2004) 71.

2-4 Determination of Nonlinear Resonance Parameters in Electron Storage Rings

The nonlinear beam dynamics of the betatron motion in a circular accelerator has been studied using analytical, numerical and experimental methods. In third-generation synchrotron light sources and colliders similar to those of the KEK B Factory, the problem is a narrow dynamic aperture caused by a nonlinear magnetic field, because strong sextupole magnets are used for chromaticity corrections. Top-up injection is carried out in some synchrotron light source facilities. Any beam loss caused by the effect of the nonlinear field must be avoided. It is essential to investigate the effect of nonlinear fields on the beam when designing and operating an accelerator.

The nonlinear betatron motion will be strongly excited when it encounters resonance conditions, in spite of the fact that the nonlinear magnetic fields are three orders-of-magnitude weaker than the linear fields in the accelerator. In general, it is not easy to completely estimate the strength of resonance phenomena in an actual accelerator theoretically, because the sources of the resonance must be introduced prior to any calculation. To understand resonance phenomena it is necessary to rely on experimental methods.

According to perturbation theory, the nonlinear Hamiltonian near the resonance can be simply described by two resonance parameters. It is important to determine these parameters experimentally for a nonlinear Hamiltonian. We demonstrate an experimental determination of the resonance parameters of a nonlinear Hamiltonian [1, 2]. Using the method the parameters can be determined precisely by studying their response to a nonlinear magnetic field. By studying the dependence of the resonance parameters on the strength of the nonlinear field, we have been able to identify the most probable origin of the resonance. Results for the fourth-order resonance $4\nu_y = 17$ are reported here.

Let us consider a model for the nonlinear betatron motion which has nonlinear betatron detuning and an n-th order parametric resonance, $n\nu_y = l$. According to first-order perturbation theory, the Hamiltonian for the betatron motion of a single particle in a circular accelerator is given by

$$H_n = \nu_y J_y + \frac{1}{2}\alpha_{yy} J_y^2 + J_y^{n/2} G_{0,n,l} \cos\left(n\phi_y - l\theta + \xi_y\right), \quad (1)$$

where ν_y represent the vertical betatron tune and (J_y, ϕ_y) are action-angle variables. Let s denote a coordinate along the longitudinal trajectory. s is given by $s = R\theta$, where R is the effective radius of curvature in the circular accelerator. In this model, the resonance pattern in phase space is described by the resonance parameters

α_{yy} and $G_{0,n,l}$. The vertical detuning parameter α_{yy} influences the amplitude-dependent tune shift, $G_{0,n,l}$ is the strength of the vertical n-th order resonance, and ξ_y is the phase of the resonance that controls the position of the resonance island in phase space.

In order to determine the resonance parameters precisely, we measured the response of the resonance pattern as a function of the strength of the nonlinear magnetic field. In the experiments, we measured the response of the resonance parameters as a function of the strength of the octupole magnetic field. In the PF ring, four octupole magnets are installed to produce the tune spread. During the experiment, we set the strength of the four octupole magnets to the same value. The detuning parameter is approximated by

$$\alpha_{yy} = \frac{1}{16\pi} K_3 \sum_{i=1}^{4} \beta_{y,i}^2 , \qquad (2)$$

where $K_3 = L_{oct} / (B\rho)\, d^3B_y / dx^3$ denotes the octupole field strength, and $\beta_{y,i}$ is the vertical betatron function at the i-th octupole magnet. Since we did not change the sextupole field strength during the measurement, the detuning parameter, which is caused only by the sextupole field, must be fixed. Therefore, the detuning parameter is presumed to be a linear function of the octupole field strength, K_3, and is given by

$$\alpha_{yy} = a_0 + a_1 K_3 \qquad (3)$$

where a_0 and a_1 are constants. Similarly, the resonance strength for the vertical fourth-order resonance $4\nu_y = l$, caused by the octupole magnets, becomes a linear function of K_3, given by

$$G_{0,4,l} e^{i\xi_y} = \frac{1}{96\pi} K_3 \sum_{i=1}^{4} \beta_{y,i}^2 e^{i[4\chi_y - (4\nu_y - l)\theta]} . \qquad (4)$$

An assumption that there is no origin of the vertical forth-order resonance besides the octupole magnets would lead to the resonance strength expressed as

$$G_{0,4,l} = g_0 + g_1 K_3 \qquad (5)$$

where g_0 and g_1 are constants. Therefore, according to first-order perturbation theory, the resonance parameters near the fourth-order resonance become linear functions of K_3.

The property of the betatron motion near the resonance appears prominently as a resonance island or separatrix in the resonance pattern. The resonance pattern is formed by turn-by-turn tracking of the motion in the y-y' phase space, as observed at a given location in the circular accelerator. We can determine the resonance parameters from the resonance pattern. In order to obtain the resonance pattern experimentally, we used fast kicker magnets to excite the initial amplitudes of coherent betatron motion. We used a phase-space monitor system for recording turn-by-turn data of y and y' [3].

The measurement near the fourth-order resonance was carried out under the following conditions. The beam current was approximately 9.0 mA, the initial betatron amplitude was $y(0)$ = 4.0 mm, and the initial betatron tunes were (ν_x, ν_y) = (9.660, 4.240). During the measurement, these parameters were fixed. The octupole field strength K_3 was varied from −390 to 390 m^{-3}, and turn-by-turn betatron motion was studied.

Figure 22 shows the vertical beam position and phase space (y-p_y) plots recorded for 16384 turns following a single kick for five different octupole field strengths. Stable islands are observed at K_3 = 208.23 m^{-3}. The vertical positions, y, are periodic appearing every four turns, and are concentrated around four specific positions.

The resonance parameters α_{yy} and $G_{0,n,l}$ were determined by the following two steps. Firstly, we evaluated the detuning parameter α_{yy} from the experimental data. The betatron tune as a function of the betatron amplitude J_y is described by $Q_y = \nu_y + \alpha_{yy} J_y$. We evaluated

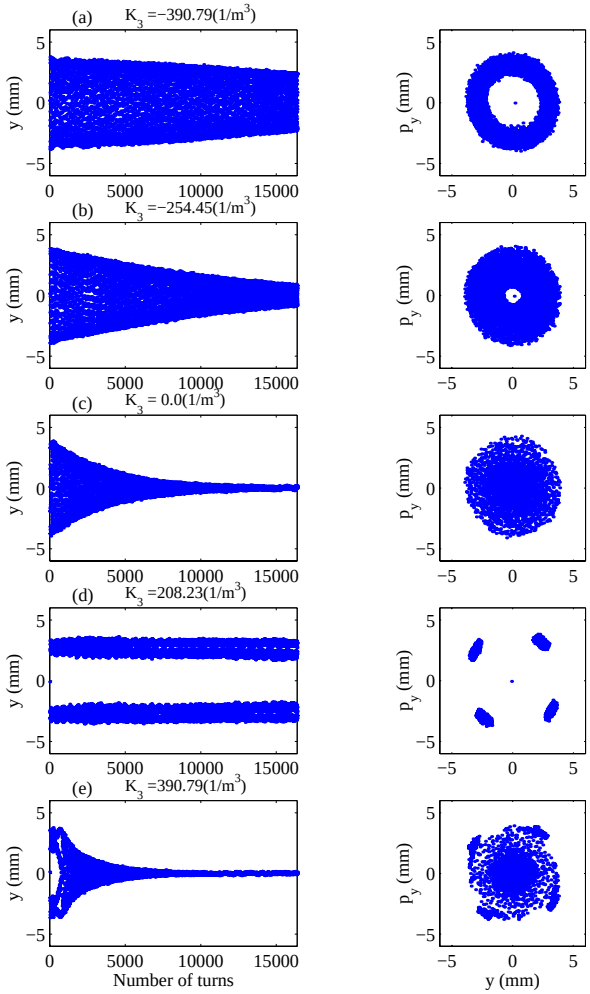

Figure 22
Plots of measured vertical positions at each revolution after a vertical kick near the fourth-order resonance at K_3 = −390.79 m^{-3}, −254.45 m^{-3}, 0.0 m^{-3}, 208.23 m^{-3} and 390.79 m^{-3}. Phase space plots (y-p_y) are also displayed [1].

Q_y from the fast-Fourier transform (FFT) of the turn-by-turn data of y, and obtained α_{yy} by fitting it to the linear function. Secondly, using the above-mentioned α_{yy}, we evaluated $G_{0,n,l}$. By fitting the turn-by-turn data of the action-angle variables (J_y, ϕ_y) to eq. (1) by the least-squares method using the above α_{yy}, we obtained $G_{0,n,l}$. In this fitting, the fixed parameter was α_{yy} and the free parameters were $G_{0,n,l}$ and H_n in eq. (1). Both α_{yy} and $G_{0,n,l}$ were determined for each K_3.

The measured α_{yy} is shown in Fig. 23. It can be seen that the measured α_{yy} is an almost linear function of K_3. The measured $G_{0,4,17}$ is shown in Fig. 24. Measured phase space (y-p_y) plots and contour plots of the Hamiltonian eq. (1) with obtained α_{yy} and $G_{0,4,17}$ at K_3=−254.45 m^{-3} and 208.23 m^{-3} are shown in Fig. 25. We can conclude that the measured $G_{0,4,17}$ is an almost linear function of K_3, similar to the measured α_{yy}. Since the dependence of $G_{0,4,17}$ was consistent with the prediction of first-order perturbation theory, we conclude that the origin of the vertical fourth-order resonance is the octupole field.

We have established a method to determine the nonlinear Hamiltonian near the resonance by experiment, and in the future we plan to determine other resonance parameters such as those for horizontal and higher-order resonances.

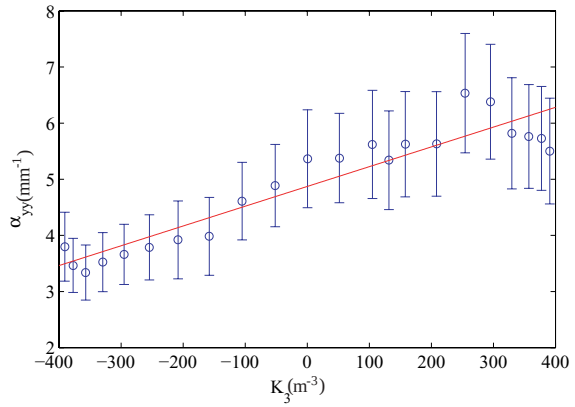

Figure 23
Dependence of the detuning parameter α_{yy} on octupole field strength K_3 for measuring fourth-order resonance. The detuning parameter is calculated from the data of Q_y and J_y. The solid line was computed using a least-squares method based on the supposition that α_{yy} is a linear function of K_3.

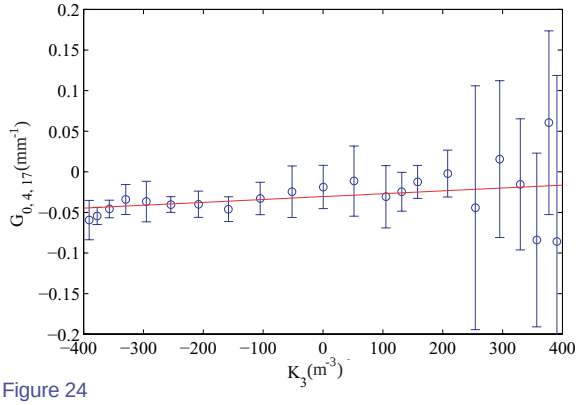

Figure 24
Dependence of the resonance strength $G_{0,4,17}$ on the octupole field strength K_3 for measuring fourth-order resonance. The solid line was computed using a least-squares method based on the supposition that $G_{0,4,17}$ is a linear function of K_3.

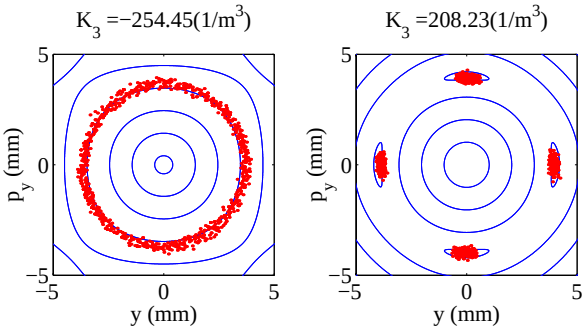

Figure 25
Fitting of experimental data to the Hamiltonian of eq. (1), at K_3 = −254.45 m^{-3} and 208.23 m^{-3} for measuring fourth-order resonance. The dots denote the experimental data and the solid curves denote the contour lines of the Hamiltonian. The resonance strengths were calculated to be $G_{0,4,17}$ = −0.0403 mm^{-1} for K_3 = −254.45 m^{-3} and $G_{0,4,17}$ = −0.0022 mm^{-1} for K_3 = 208.23 m^{-3} using a least-squares method.

References

[1] T. Miyajima and Y. Kobayashi, *Jpn. J.Appl. Phys.*, **4A**, 2006 (2005) 44.

[2] T. Miyajima and Y. Kobayashi, *J. Particle Accel. Soc. Jpn,* **1** No. 2 (2004) 98.

[3] Y. Kobayashi, T. Mitsuhashi, A. Ueda and T. Kasuga, *Proc. Fifth European Particle Accelerator Conf.*, *Sitges, Spain*, (1996) 1666.

2-5 Beam Position and Angle Monitor by Using SR Monitor Technique

Monitoring the beam position and angle in the the undulator is still one of important problems in the SR facilities. In our previous work [1], for the separation of the undulator radiation from the bending radiation, we applied a focusing system similar to that used in the visible SR profile monitor. The position of the electron beam inside the undulator was measured by measuring the position of beam image. The performance of this monitor was tested by using the BL-5 undulator beamline. In the present work, a second optical system is added for a measurement of an angular variation of the electron beam. To measure an angular variation of the electron beam is just same problem as to measure an angular variation of optical axis of SR from the source point. Since the afocal system like a Kepler type telescope [5] converts an angular variation of optical axis of input ray into a positional variation, we can measure an angular variation through a positional variation of a light spot on the CCD camera. We tested this monitor at the SR monitor beamline at BL-27 (bending source) instead of BL-5 due to a serious floor vibration problem at the BL-5. For this monitor, there exists no difference between undulator source and bending source except separation technique [1].

Two types of optical systems were used for the observation of position and angle of the electron beam. One is a focusing system to make an image of the electron beam for the observation of its position. The

other is so called an afocal system for the observation of angle of the electron beam. The setups of both optical systems are illustrated in Fig. 26.

Let us denote the transverse magnification of the focusing system (a) by β, then the angular magnification γ is given by $\gamma = 1/\beta$. The normal arrangment of the focusing system employs a larger transverse magnification for observing the image or its position. Oppositely, the angular magnification is smaller in this system than in the normal one. At the present time, we set a transverse magnification $\beta = 10$. In the afocal system, a small transverse magnification will be set for the focusing system in the first stage of the total system to increase an angular magnification. In the next stage of the focusing system, a collimating lens is arranged so as to make the afocal condition. As shown in Fig. 27, the angular variation θ of input optical axis is converted into a positional variation x of the optical axis on the CCD camera. Namely, x is given by

$$x = d \cdot \theta,$$

where d is the distance between the focal plane of the first stage optics and the collimating lens.

An angular variation in the optical axis is converted into a positional variation in this stage. In the present case, we set an angular magnification $\gamma = 200$ for the first stage focusing system. Since the transverse magnification is 1/200, we can neglect a positional variation of the image at the focal plane of the first stage optics. The focal length of the collimating lens is 50 mm. With this condition, an angular variation 50 μrad will give a position variation 0.5 mm on the CCD camera. The spectrum of the input light for both the system is limited to 10 nm at 550 nm by a band-pass filter. The σ−polarization component was selected using a dichroic sheet polarizer. The results obtained by the focusing system and the afocal system are shown in Fig. 28.

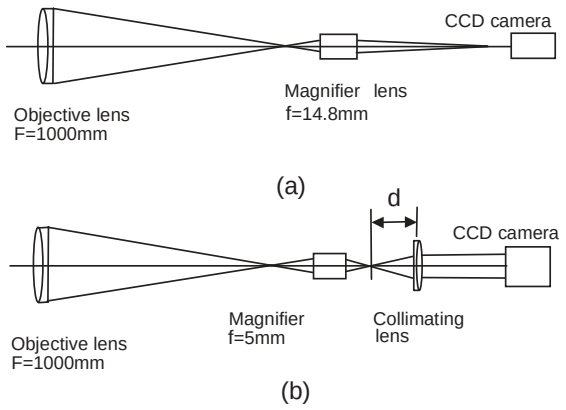

Figure 26
Focusing system (a) for observation of the beam position and afocal system (b) for observation of beam angle.

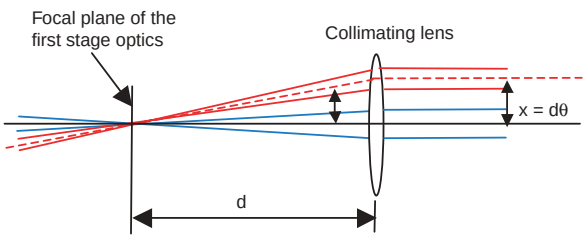

Figure 27
Collimating section in the afocal system.

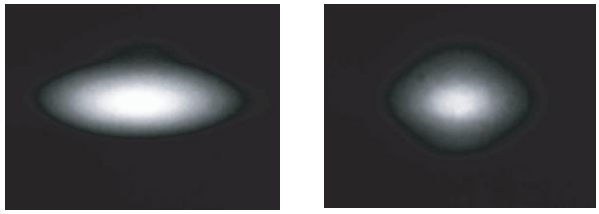

Figure 28
Electron beam images produced by the focusing system (a), and intensity distribution of the light beam at the afocal system (b).

Calibration of the system is necessary to know the absolute values of the positional variation and angular variation of the electron beam. In a previous work [2], an optical beam shifter was used for the calibration of transverse positions of the electron beam. In the present work, a movable mirror which is set at 3 m downstream from the source point is used for calibration of both the positional variation and angular variation of the electron beam. The positional variation Δρ and angular variation Δφ are given by the following equations,

$$\Delta\rho = 2 \cdot L \cdot \theta,$$
$$\Delta\phi = 2 \cdot L,$$

where L denotes the distance between the source point and the mirror, and θ denotes the rotation angle of the mirror. Since two optical systems have a rotational symmetry around the optical axis, calibration factors for the vertical and the horizontal direction must be the same. But actually, aspect ratio of the CCD camera is not precise sufficiently. We calibrated both of the vertical and the horizontal directions via step-scanning of the mirror

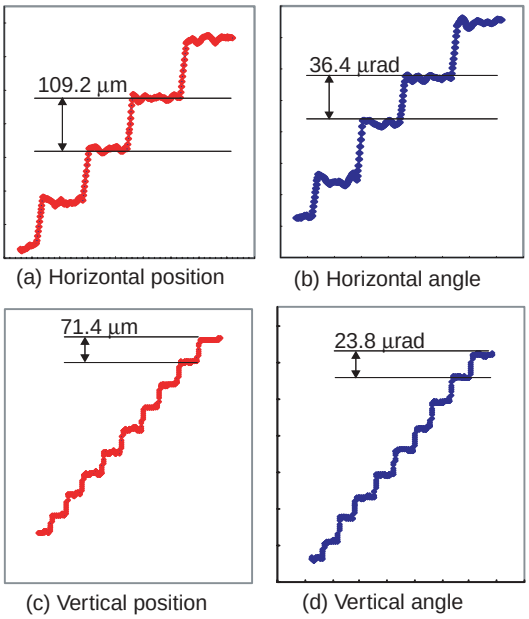

Figure 29
Results of calibration; (a) horizontal position, (b) horizontal angle, (c) vertical position, (d) vertical angle.

in both directions. The results of the calibrations are shown in Fig. 29.

The position sensing of the spots of the light beam on the CCD camera in this calibration was performed by two steps; 1) to make vertical and horizontal projections of the beam spot, 2) to analyze the positions of each projections by fitting a Gaussian profile with the least-squire-fitting method. The scanning steps of the mirror in the vertical and the horizontal directions were 11.9 μ rad and 18.2 μrad, respectively. The steps of angular variations are twice these angles, namely 23.8 μrad in the vertical and 36.4 μrad in horizontal. Corresponding steps of the beam-position variations in the vertical and the horizontal are 71.4 μm and 109.2 μm, respectively.

The monitor is experimentally operated at BL-27. The positional variation and angular variation of the electron beam are continuously recorded by every 1 s. Two examples of 24-hour recording of the positional variations and the angular variations are shown in Fig. 30.

Since the electron beam is injected into the ring twice a day, the positional variation and angular variations in Fig. 30 exhibit two discontinuous changes within the 24-hour period. In the example (a), a sudden change in the horizontal position and angle was observed at two hours after the injection. A similar sudden change is not observed in the example (b). In the example (b), the effect of a temperature change in the ring tunnel was observed as a vertical angular variation. Large fluctuations in the beam positional variation were observed in the example (a) compared with the example (b). In both the cases, a tendency to a systematic drift in the data was also observed.

By combining with the technique to observe the undulator source point in a previous work [4], this monitor is fully applicable to the observation of the electron beam position and angle in the undulator. This monitor can also provide direct information about the electron beam position and angle at the bending source. The time interval for data taking is typically 1 s. If the CCD camera is replaced by faster devices such as a four-quadrant photodiode, this monitor can work like a phase-space monitor. On the other hand, a systematic drift in the data was observed with this monitor. We attribute the drift to some systematic motion existing between the source point and the optical system. The monitor will be installed in BL-17 whose light source is a short-period undulator.

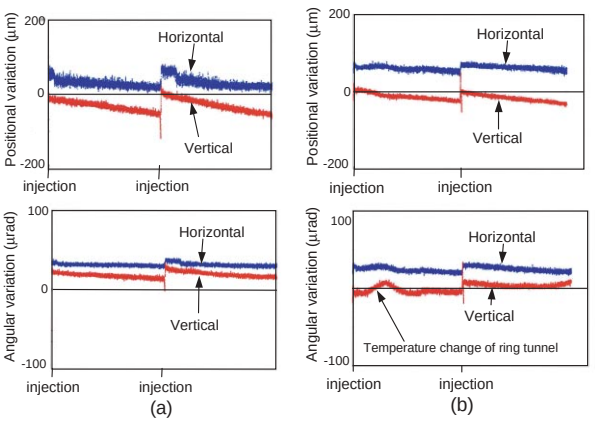

Figure 30
Two examples of 24-hour recordings of beam positions and angles.

References

[1] T. Mitsuhashi and M. Tadano, *PAC'05, Oakridge*, (1996) 2789.

[2] D. J. Schroeder, "Astronomical Optics", Academic press, (2000) 131.

2-6 Commissioning and First Operation of the Short-Gap Undulator SGU#17

The Straight-Section Upgrade Project of the Photon Factory (PF) ring has been completed in FY2005 [1]. The upgrade has produced four new 1.4-m-long straight sections, with other existing ones being nearly doubled in length. The 1.4-m-long straight sections were designed to have small betatron functions, so as to enable the installation of in-vacuum-type undulators with a very short magnetic period and gap.

Even with a beam energy of 2.5 GeV of the PF ring, it is possible to utilize hard X-rays up to 15 keV if we select the lower harmonics (below 7th) of radiation emitted from an undulator with a very short period length**.** However, this is valid only if the undulator can be set to a very short gap of the order of 5 mm or less to obtain sufficiently high field strength. This requirement is fulfilled by a combination of the in-vacuum undulator technology [2, 3] and advanced lattice design including small betatron functions [4].

This led us to develop a short-period, small-gap undulator (SGU) in the in-vacuum configuration [5]. The undulator, named SGU#17, was installed at the new straight section between bending magnets B#16 and B#17 in the up-graded PF lattice. This is one of the four new 1.4-m-long straight sections. The comparative layout of the 1.4-m-long straight section before and after the upgrade is illustrated in Figs. 31(a) and 31(b), and the optical functions shown in Fig. 31(c). The vertical betatron function was designed to be 0.4 m at the center of the section to allow a minimum gap of 4.5 mm.

For construction of SGU#17, we employed a pure Halbach-type magnet arrangement, and tried two different sets of magnet arrays with period lengths (λ_u) of 12 and 16 mm in investigating short-period undulator magnets. The allowable length at the installation site led us to adopt a periodicity (N) of 39 for λ_u=12 mm, and N = 29 for λ_u=16 mm. Finally we chose a period length of λ_u=16 mm in order to satisfy the users' requirements, mainly with regards to the available photon energy region. The magnet material was selected to be Nd-Fe-B alloy with a remanent field of B_r=12.0 kG and a coerciv-

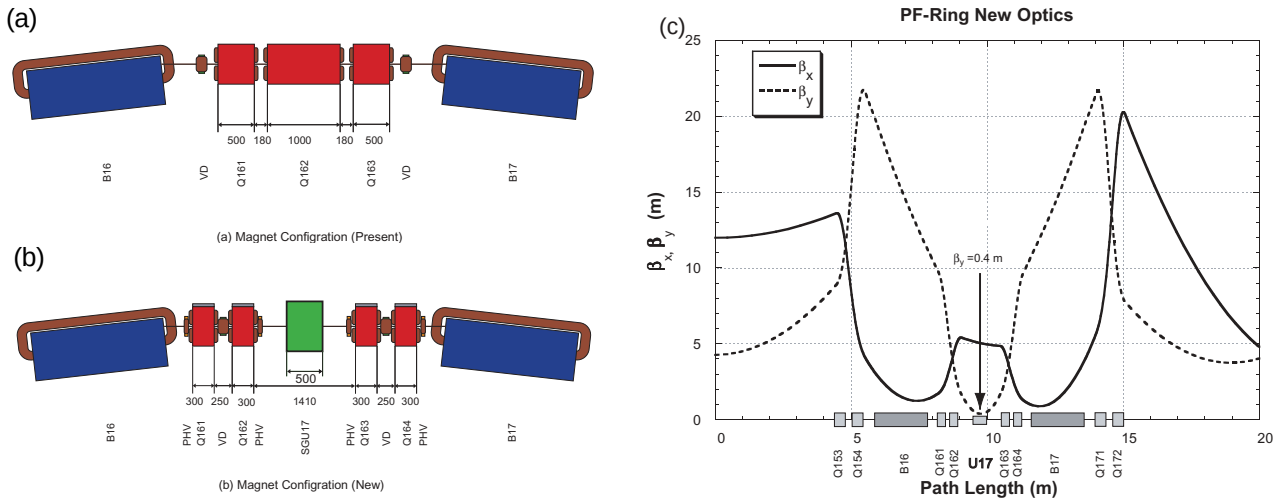

Figure 31
Comparative layout of the 1.4 m straight section before (a) and after (b) reconstruction. The vertical betatron function (c) was designed to be 0.4 m at the center of the section.

ity of iH_c=28.0 kOe (NEOMAX35VH manufactured by NEOMAX Co. Ltd.), because of its excellent magnetic performance and endurance against high temperatures during baking. Magnet blocks made of the porous material were coated with 5-μm-thick TiN for vacuum sealing. They were embedded in an oxygen-free-copper holder, and attached to a pair of magnet-mounting beams made of Al alloy.

The magnet system components were mounted in a vacuum chamber made of stainless steel with a size of 250 mm (inner diameter) × 980 mm. The inner surface of the chamber was electrolytically polished. The vacuum chamber was evacuated with a combination of Ti sublimation pumps (TSP) and sputter ion pumps (SIP). Using this pumping system resulted in a pressure of 7.5 × 10^{-10} Torr following baking at 120°C for 48 hrs. The magnet gap ranges from 40 mm to 4.5 mm with the deflection parameter K ranging up to 1.27 for the magnet arrays with λ_u=16 mm, and 0.72 for λ_u =12 mm. The gap is changed by a translation system composed of precise ball screws and linear guides. The translation system movement is transmitted to the magnet arrays through linear-motion feedthroughs using bellows couplings. In order to avoid problems due to Ohmic and parasitic mode losses, we covered the opposing faces of the magnet arrays with thin metal foils. The foil used was 60 μm in thickness and made of oxygen-free copper plated with 25-μm-thick Ni for magnetically sustaining the foil on the magnet face.

A contactor composed of a 180-μm-thick Be-Cu foil was attached for flexibly connecting the end of the magnet array to a Q duct of the PF ring. This type of flexible contactor was developed for the in-vacuum undulator, U#NE3, installed in the 6.5-GeV PF-AR [2].

In order to avoid problems due to Ohmic losses at the contactor when the SGU is set to a very short gap (5 mm or less), we have attached a water-cooling pipe to the base block of the contactor. Heat due to Ohmic losses caused by the image current in the contactor can be removed by heat conduction through this oxygen-free copper block. The internal structure of SGU#17 is shown in Fig. 32.

The magnetic fields have been adjusted on the basis of precise field measurements. For this purpose, we have devised a new magnetic detector using Hall probes which are oriented in the y- and x- directions as shown in Fig. 33. The sensor part of the detector was designed to fit in a gap as short as 3 mm. This part is a kind of a Cu micro-oven equipped with a thermistor-type thermometer and heaters. The temperature can be

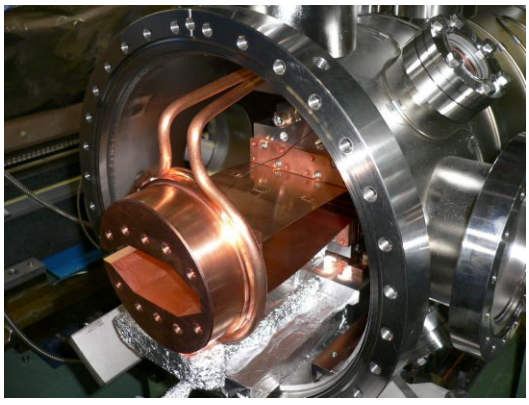

Figure 32
Internal structure of SGU#17. The end of magnet arrays and the flexible contactor are shown.

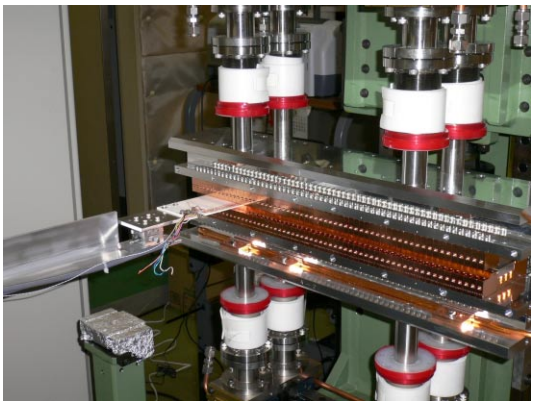

Figure 33
SGU#17 magnet under field adjustment.

controlled with an accuracy of 0.01°C [6]. The undulator field was adjusted by optimizing the kick angle of the electron beam at each pole to finally produce an ideal sinusoidal orbit in the horizontal plane and a straight orbit in the vertical plane. Our adjustment method employs: (1) the exchange of the magnet blocks and (2) the insertion of disk-shaped magnet chips into the holders of the magnet blocks.

Figure 34 summarizes the electron orbits in the undulator for λ_u=16 mm. The quality of the undulator fields was found to be high over the whole range of the gap, although the field adjustment was carried out only at a gap of 5 mm. Satisfactory results have been obtained on the kicks at the undulator's entrance and exit that violate parallelism between the electron orbit and the undulator central axis. The absolute values of both the kicks and their relative changes were found to be sufficiently small. Figure 34 shows the kicks at the entrance as a field integral, BS_{ENT} (G·cm). The effects of the field errors on each harmonic radiation can be described by the ratio of the real brilliance of the radiation to the ideal brilliance. The real brilliance is calculated for a single electron using the measured field data, whereas the ideal one is calculated for a field without errors. Fine field adjustments for SGU#17 (λ_u=16 mm) resulted in a brilliance ratio as high as 94% for the fifth harmonic**.** For the magnet array with λ_u=12 mm, this ratio amounted to 96% for the third harmonic.

SGU#17 was installed in the PF ring in June 2005 (Fig. 35). The PF ring was recommissioned in Septem-

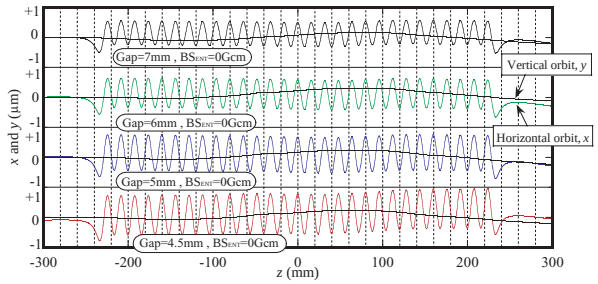

Figure 34
Summary of the field adjustment of SGU#17 (λ_u=16mm). *x* (horizontal) and *y* (vertical) orbits are shown at several gaps. BS_{ENT}s denoting field integrals at the entrance part of SGU#17 are negligibly small.

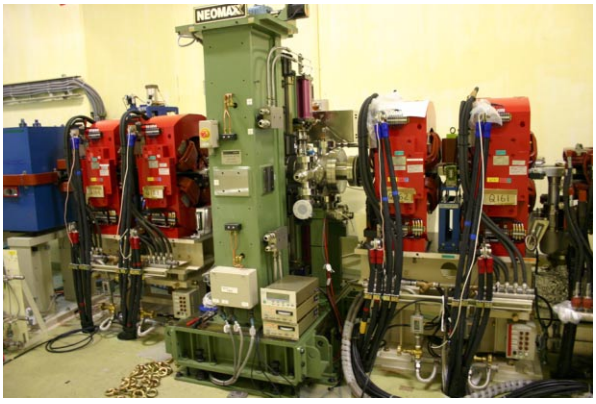

Figure 35
Installed SGU#17.

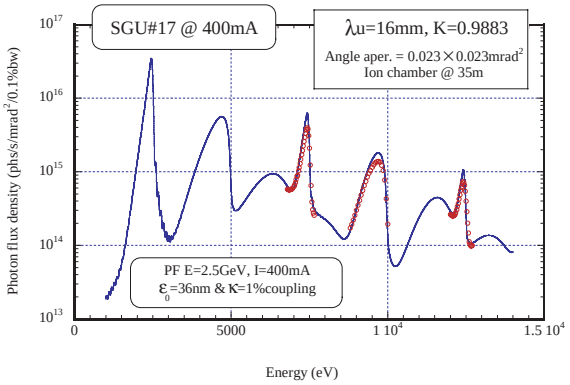

Figure 36
Undulator spectrum of SGU#17: a tentative version. Comparison between observation (circles) and calculation (a solid curve) is shown.

ber 2005 following the upgrade which had been made during the half-year shut-down of the ring [1]. SGU#17 itself and the associated beamline [7] were subsequently commissioned. During the comissioning process we found that the allowable minimum gap of SGU#17 is 3.8 mm, compared to the designed value of 4.5 mm. The gap of SGU#17 can be tuned independently of the operation of the PF ring without using any orbit correction. The orbit differences in both the *x*- and *y*-directions were found to be less than 5 μm throughout the whole ring when decreasing the gap from the maximum (40 mm) to 4 mm.

Characterization of the radiation emitted from SGU#17 is now underway at the beamline. Preliminary results of the spectrum measurements are shown in Fig. 36. We have used a cryogenically-cooled Si double-crystal monochromator and a 2-dimensional slit for the measurements. The 2-dimensional slit was placed at a position 35 m away from the source with its aperture being 0.8 mm × 0.8 mm. The photon flux was determined using an ion-chamber detector. Figure 36 shows the results for the 3rd, 4th and 5th harmonics of the undulator radiation for *K*=0.9883. The spectral peak height was normalized to a beam current of 400 mA. The solid curve represents the spectrum expected from the designed parameters of the PF ring following recommissioning.

References

[1] T. Hond, et al., *Proc. SRI2006, Daegu, Korea* (2006).
[2] S. Yamamoto, T. Shioya, M.Hara, H. Kitamura, X. W. Zhang, T. Mochizuki, H. Sugiyama and M. Ando, *Rev. Sci. Instrum.* **63(1)** (1992) 400.
[3] S. Yamamoto, K. Tsuchiya and T. Shioya, *AIP Conference Proc.*, **705** (2004) 211.
[4] Y. Kobayashi, Photon Factory Activity Report 2003 **20** (2004) 98.
[5] S. Yamamoto, K. Tsuchiya and T. Shioya, *Proc. SRI2006, Daegu, Korea* (2006).
[6] S. Yamamoto, T. Shioya, H. Kitamura and K. Tsuchiya, *Rev. Sci. Instrum.*, **66(2)** (1995) 1996.
[7] N. Igarashi et al., *Proc. SRI2006, Daegu, Korea* (2006).